land

MDPI

Article

Analysing Land Cover Change in the Valencian Community through Landsat Imagery: From 1984 to 2022

Jose Antonio Sobrino *, Sergio Gimeno, Virginia Crisafulli and Álvaro Sobrino-Gómez

Global Change Unit, Image Processing Laboratory (IPL), University of Valencia, E-46980 Paterna, Spain; sergio.gimeno-crespo@uv.es (S.G.); virginia.crisafulli@uv.es (V.C.); alvaro.sobrino@uv.es (Á.S.-G.)
* Correspondence: sobrino@uv.es

Abstract: Land cover change represents one of the most significant global transformations, which has profound impacts on ecosystems, biological diversity, and the ongoing climate crisis. In this study, our objective was to analyse land cover transformation in the Valencian Community over the last four decades. Utilising Landsat 5, 8, and 9 summer images, a Random Forest algorithm renowned for its ability to handle large datasets and complex variables, was employed to produce land cover classifications consisting of five categories: 'Urban Areas', 'Dense Vegetation', 'Sparse Vegetation', 'Water Bodies', and Other'. The results were validated through in situ measurements comparing with pre-existing products and utilising a confusion matrix. Over the study period, the urban area practically doubled, increasing from approximately 482 to 940 square kilometres. This expansion was concentrated mainly in the proximity of the already existing urban zone and occurred primarily between 1985 and 1990. The Dense and Sparse Vegetation classes exhibit substantial fluctuations over the years, displaying a subtle trend towards a decrease in their cumulative value. Water bodies and Other classes do not show substantial changes over the years. The Random Forest algorithm showed a high Overall Accuracy (OA) of 95% and Kappa values of 93%, showing good agreement with field measurements (88% OA), ESA World Cover (80% OA), and the Copernicus Global Land Service Land Cover Map (73% OA), confirming the effectiveness of this methodology in generating land cover classifications.

Keywords: land cover; Landsat; change detection

check for updates

Citation: Sobrino, J.A.; Gimeno, S.; Crisafulli, V.; Sobrino-Gómez, Á. Analysing Land Cover Change in the Valencian Community through Landsat Imagery: From 1984 to 2022. *Land* **2024**, *13*, 1072. https://doi.org/10.3390/land13071072

Academic Editor: Karel Charvat

Received: 21 June 2024
Revised: 10 July 2024
Accepted: 15 July 2024
Published: 17 July 2024

1. Introduction

Enhancing our comprehension of the Earth's surface coverage is pivotal for a wide range of activities and applications. These encompass urban and regional planning [1], environmental impact assessment [2], global warming mitigation [3,4], and the monitoring of natural phenomena [2,5,6].

This type of research facilitates improved management and understanding of the ongoing transformations [7], aiming at their preservation. These changes exert a substantial impact not only on the environment and climate [8,9] but also on human society. This impact manifests in the depletion of ecosystem services [10]; heightened susceptibility to extreme events like floods, landslides, and droughts [11]; and environmental degradation [12], among other consequences.

The generation of land cover maps using satellite images offers significant advantages due to their economic efficiency, rapidity, and extensive coverage in both time and space [13]. Consequently, the creation of this type of product stands out among the fields of application of Remote Sensing (RS) technology [14–16].

In recent years, the application of machine learning algorithms has garnered considerable attention in ecological research [10,17–19]. The use of this technique spans numerous geoscience topics, including extreme weather pattern analysis, climate change projections, precipitation nowcasting, and carbon flux prediction. Additionally, it plays a significant role in image fusion, registration, change detection, image segmentation, and drought forecasting [20]. These algorithms facilitate the classification of satellite-acquired information based on clearly identifiable characteristics, resulting in a product that identifies the different land cover types designed for specific end uses [21].

Among the array of algorithms available, Random Forest (RF) is one of the most widely employed [10,22–24]. Renowned for its robust classification methodology [25], RF excels in producing accurate maps for complex land cover categories [26], handling noisy data [24,27,28] at relatively modest computational costs [29,30]. Moreover, its non-parametric nature and effectiveness with limited datasets compared to study area size make it an ideal candidate for this type of analysis [17,23,26,31].

The Google Earth Engine (GEE) platform, launched by Google in 2010, enables the analysis of a huge amount of data in a short time [32], allowing the general public to process large quantities of satellite information. With its impressive computational capabilities and a broad range of available RS products encompassing both raw and processed data, GEE has swiftly emerged as one of the most utilised platforms in this field [33].

This research presents a quantitative analysis of land cover change from 1984 to 2022, using Landsat, one of the most widely used satellite constellations in this area [34,35] due to its spatiotemporal resolution, suitable for studying regional land transformations. By selecting the entire Landsat series, we can effectively study the evolution of land cover change over an extended period, spanning nearly 40 years from the earliest to the most recent date. This long-term perspective allows for a comprehensive analysis of trends and patterns, providing valuable insights into the dynamics of land cover transformation. We choose to conduct the study in the Valencian Community, a region with unique ecosystems of strong environmental importance. We ensured the accuracy of our classification results by comparing them with field measurements and existing datasets from the Copernicus service and European Space Agency (ESA).

The detailed account of land cover changes presented here provides essential insights for policymaking, delivering a comprehensive overview of land cover alterations within the Valencian Community over the past four decades. The document is structured as follows: Section 2 will delve into the classification and validation methodology, Section 3 presents the obtained results, Section 4 discusses the data, and finally, Section 5 offers concluding remarks.

2. Materials and Methods

2.1. Study Area

The Valencian Community (Figure 1), situated along the eastern coast of Spain, holds significant economic and cultural prominence. Positioned at approximately 39° north latitude and 0° west longitude, overlooking the Mediterranean coast, this region has experienced substantial transformations in land cover, primarily due to urban expansion and agricultural development. This characteristic renders it an ideal subject for our study, which seeks to explore the dynamic shifts in land cover, elucidating the evolving urbanisation patterns and their interaction with the natural environment.

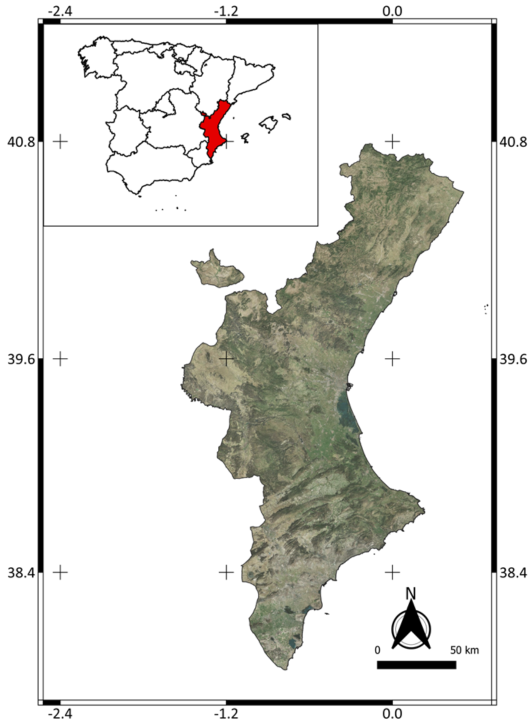

Figure 1. Satellite view of the Valencian Community. In the upper-left: a detailed view of Spain.

2.2. Input Data

For over four decades, the satellite constellation Landsat has provided valuable information on the state and dynamics of our planet, providing images with high spatial (15 m, 30 m and 100 m, depending on the bands) and temporal resolutions (8 days, with 16 observations per satellite and two satellites per mission). Other missions, such as Sentinel-2, either lack a comparable long time series or, like MODIS, do not boast a high spatial resolution. Furthermore, since the images became freely accessible in 2008, this satellite has emerged as one of the most widely utilised [34,36,37], with applications ranging from planning and monitoring to surveillance [35,38–40]. Given its extensive time coverage, this satellite constellation aligns seamlessly with our study objectives, enabling the monitoring of land cover changes over the longest available timeframe.

In this study, we employed the following datasets via GEE platform: 'LANDSAT/LT05/C02/T1_L2', 'LANDSAT/LC08/C02/T1_L2', and 'LANDSAT/LC09/C02/T1_L2', corresponding to the atmospherically corrected level-2A products of Landsat 5, 8, and 9. Its known issues with image acquisition disturbances motivated the deliberate exclusion of Landsat 7.

To reduce the probability of encountering cloudy pixels in the images and to mitigate the impact of pronounced seasonal variations, only summer images, acquired from June 1st to September 30th, were analysed. Landsat 5 images were used for the years 1984, 1985, 1990, 1995, 2000, 2005, and 2010; while Landsat 8 images were used for the years 2015 and 2020; and Landsat 9 was used for 2022 and 2023 (Table 1).

We have chosen a series of five-year intervals to observe land cover changes within a relatively short time span, ensuring the analysis remains manageable and effective. Additionally, an analysis for the year 1984 was conducted, marking the beginning of the Landsat series, to allow for direct comparison with the most recent years, 2022 and 2023, the latter being used for validation purposes.

Table 1. Summary of the total training points used to classify each year, employing both Random Forest and Classification and Regression Trees algorithms. The data points are categorised by land cover classes, and details regarding the satellite used, along with the total number of images for each year, are specified.

Satellite	Year	Images	Built-Up Area	Water Bodies	Dense Vegetation	Sparse Vegetation	Other
Landsat 5	1984	35	239	121	983	1023	59
	1985	38	126	60	614	535	38
	1990	60	214	37	750	490	43
	1995	48	273	74	1063	1051	110
	2000	42	247	31	1052	723	32
	2005	45	212	34	760	754	42
	2010	45	270	86	1137	862	37
Landsat 8	2015	58	321	71	1196	850	24
	2020	57	440	77	1013	641	65
Landsat 9	2022	57	395	50	1345	930	34
	2023	28	236	44	761	497	45

2.3. Algorithm

2.3.1. Random Forest

RF is an accurate and computationally efficient technique capable of swiftly processing extensive datasets [25,41]. It is an extension of Classification Tree Analysis (CTA), frequently employed in the analysis of remotely sensed data for generating land cover classifications.

In each classification tree, the input data (the pixels) undergo a hierarchical partitioning into increasingly homogeneous groups corresponding to different land cover classes based on their relationships with a set of predictive variables (the spectral bands) [23,42]. The model is then trained using the spectral band responses to produce an output map displaying potential land cover classes. Each decision tree node utilises a randomly selected subset of attributes from the original set, promoting diversity in the model. Moreover, the decision trees are constructed using random yet equally sized subsets of data, and the final class assignment for a pixel is determined by a majority vote [41].

This method is simple to apply, as it has few parameters and is easy to interpret [43]. However, although the RF is robust to outliers and overfitting [25,44], it is unstable and allows small changes in the input to produce very different decision trees.

In this study, the classification was carried out for the Valencian Community area, using more than 1000 points for each year for training (Table 1). Due to the large amount of information to be analysed, all processing was performed via GEE. To implement the algorithm, we used the SmileRandomForest function, a Classifier package that handles supervised classification by traditional machine learning algorithms. GEE's RF classifier offers various customisation options, such as the number of decision trees to create, the size of the input subset per tree, and the maximum number of parent nodes for each tree. The algorithm was applied using 150 decision trees in order not to excessively increase the computational cost while maintaining good accuracy, as recommended by Oshiro et al. [41]. Default values were maintained for the other parameters.

Although some authors question the accuracy of the manual approach [45], compared to unsupervised and object-based methods, RF is equally accurate with Earth observation images at medium spatial resolution [46]. Furthermore, in our case, it would have been impossible to carry out a supervised segmentation as proposed by Stefanski et al. [47] due to the heterogeneity of the landscape and the low spatial resolution of the pixels compared to the dimensions of the objects.

2.3.2. Classification and Regression Trees

To facilitate a comparison between algorithms and subsequently determine the most efficient one, land cover was also computed using the Classification and Regression Trees (CART) algorithm developed by Breiman [48].

The CART algorithm adopts a conventional classification approach, which remains prominent despite the development of various classification algorithms [49]. This methodology addresses a range of performance, precision, and operational issues encountered by many decision tree methods [50], including challenges like determining the appropriate tree size and handling missing values. Employing a strictly binary subdivision, CART maximises the homogeneity of subsets until the node achieves the maximum possible homogeneity. When no further split enhances homogeneity, the process stops, and the node becomes terminal. The prediction is made based on these terminal nodes, determining the class [48].

The algorithm was applied using the same procedure and training points as the RF algorithm (Table 1) to ensure comparability between the classifiers. Another GEE function, named smileCart and part of the same Classifier package, was utilised for this purpose.

2.4. Process Description

In our analysis, atmospherically corrected images (level 2A) were converted from reflectivity to reflectance values, utilising the scaling coefficients provided in the product documentation, and clouds and cloud shadows were masked by employing the Quality Mask (QA band).

Given the 8-day temporal resolution of Landsat missions, we adopted a multi-month approach to ensure comprehensive coverage of our study area while eliminating any potential pixel blurriness and increasing map accuracy, as recommended by various studies [15,51,52]. Whenever multiple high-quality images were available for a specific area, we calculated the median of these images. To create a cohesive dataset, we pasted together the selected images and subsequently delimited the study area using the boundaries outlined by the Valencian Cartographic Institute for the year 2022.

For the training dataset, we manually handpicked specific pixels and assigned them to their respective classes. Our classification system consisted of five distinct categories: Water Bodies, comprising rivers, lakes, and artificial reservoirs; Built-up Areas, encompassing settlements, roads and industrial buildings; Dense Vegetation, including forests and irrigated crops; Sparse Vegetation, covering mowed crops, scrub and bushes, often accompanied by soil components; and Other, representing riverbeds, beaches, and rock mines.

These classes were selected due to their distinctiveness at a 30 m spatial resolution. The positioning of training points relied on the reference of RGB images constructed from bands 3, 2, and 1 for Landsat 5 and bands 4, 3, and 2 for Landsat 8 and 9. Thirty per cent of these points were reserved for validation purposes. To assess efficiency, the accuracy and kappa values of the algorithms were compared. Despite recent criticisms of the kappa metric for its limitations in map studies [53], we have chosen to use it due to its widespread acceptance and ease of comparison with previous studies. A flowchart illustrating the entire procedure is shown in Figure 2.

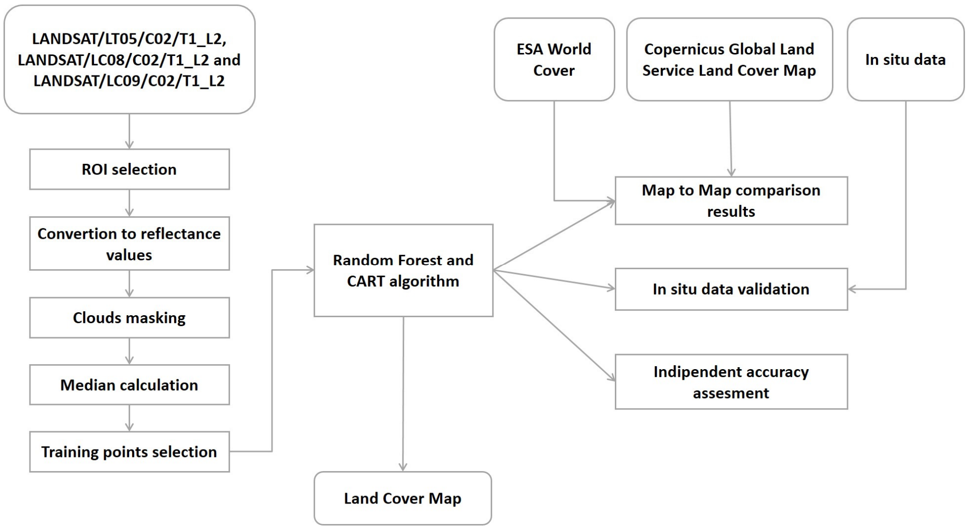

Figure 2. Flowchart of the methodology applied in this work to obtain land cover maps.

For a comprehensive understanding of urban changes, we conducted a comparative analysis of Built-up Areas class maps from 1985 to 2020. The resulting map was colour-coded to distinguish urban areas across different years, highlighting urban construction expansion. Additionally, linear regression analyses were performed for each class type over the period from 1984 to 2022 to further explore temporal trends. All statistical analyses were conducted using Python, version 3.12.

2.5. Validation

In this research, various validation methods were employed to assess the algorithm's effectiveness, aiming to evaluate its robustness and generalisability. Initially, we validated the model's performance using actual surface cover data for the year 2023. Subsequently, a validation approach involving a 70–30% split for training and testing was applied to all examined years, with the confusion matrix computed for each.

Moving to 2015, a comparison was made with the Copernicus Global Land Service Land Cover data, available exclusively for the years 2015 to 2019. For 2020, our results were then compared with the WorldCover map generated by ESA, which is applicable for the years 2020 and 2021.

2.5.1. Algorithm Validation Using Field Points

To validate the model, we calculated a land cover map utilising Landsat 9 images acquired in September and October 2023. A subset of 126 points, representing approximately 5% of the training pixels for each class, was selected from this land cover map for comparison with field data. Our rationale for selecting this subset was to ensure it would adequately represent the majority of the data's variance, thereby validating the algorithm's performance (Figure 3).

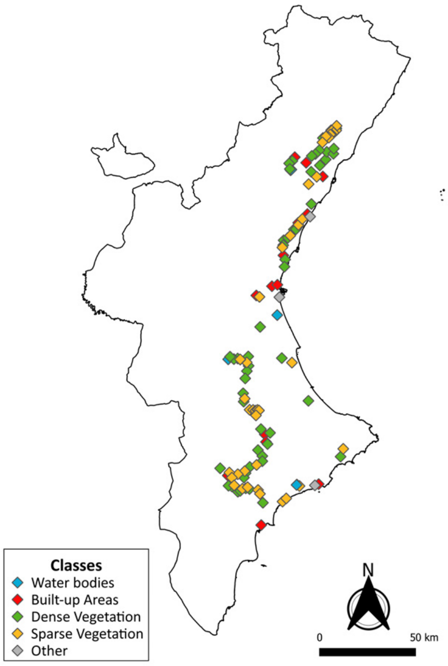

Figure 3. Map of the validation points collected along the Valencian Community.

In order to achieve this objective, the validation points were selected based on their homogeneity and large spatial extent, considering that Landsat images have a resolution of 30 m. This careful selection ensures the reliability and robustness of the validation process, which is critical for the accuracy of our analysis. The comparison was conducted visually in the field on the 30th and 31st of October, 2023.

2.5.2. Holdout Validation

To further evaluate the algorithm's performance, we divided the point dataset into two distinct subsets: a training set and a testing set. This partitioning was accomplished through a random split, assigning 70% of the data for training and reserving 30% for testing purposes.

The choice of these specific percentages is grounded in the widely recognised efficacy of the 70–30% split. This configuration consistently yields lower mean standard errors, ensuring a high precision in our analysis. This statistical advantage has been well-established in previous research, as demonstrated by Adelabu et al. [54]. The 70-30 ratio allows the detection of data patterns within a sufficiently large training set while retaining a substantial test set for a reliable estimate of the model's performance. In other words, this ratio was chosen to maintain a balance between reducing bias and controlling model variance. A smaller test set might not yield reliable performance estimates, while a larger training set could lead to overfitting, where the model excels on training data but underperforms on new data.

The test set was then utilised to compute a confusion matrix and standard performance evaluation metrics, including OA, user and producer accuracy, and the kappa coefficient [55]. OA serves as a comprehensive gauge of the total classification accuracy, essentially reflecting the likelihood of correctly classifying a randomly selected location on a map [56]. Producer's accuracy and User's accuracy are distinct metrics used to assess classification accuracy. Producer's accuracy denotes the probability that a real-world feature is accurately represented on the map, while User's accuracy signifies the probability that a class depicted on the map actually exists in the real world. The Kappa coefficient offers quantification of how superior the classification performed compared to the probability of randomly assigning pixels to their correct categories, providing a valuable indicator of classification quality [57].

2.5.3. Comparison with ESA WorldCover

The WorldCover project marks a groundbreaking initiative, offering finely detailed global land cover information at a remarkable 10 m resolution, with an estimated OA hovering around 75% [58]. This dataset, derived from Sentinel-1 and Sentinel-2 satellite observations, is available for the years 2020 and 2021.

In our research, we assess the congruence between our product for the year 2020 and the one computed by ESA for the same year. ESA's product comprises eleven distinct land cover categories, which we have grouped to simplify the comparison process. We categorised Tree Cover, Shrubland, Mangroves, Moss and Lichen, and Herbaceous Wetland classes as Dense Vegetation. Sparse Vegetation encompasses the Grassland and Cropland classes, while Built-up Areas represent the Built-up class. Water Bodies include the Snow and Ice and Permanent Water Bodies classes, and the Bare/sparse Vegetation class falls under the category of Other. Additional information on the classes and the product can be found in the User Manual edited by Zanaga et al. [58].

2.5.4. Comparison with Copernicus Global Land Cover

The Copernicus Global Land Service (CGLS) annually delivers a dynamic global land cover product, CGLSLC100, with a spatial resolution of 100 m. The third collection of this product, spanning from 2015 to 2019, is derived from PROBA-V satellite observations and ancillary datasets [37,59,60] and has an estimated accuracy of approximately 80% [60,61]. It comprises a total of 23 classes that we reorganised to facilitate comparison with the 2015 product obtained through our methodology. We grouped closed forest classes, open forest classes, scrubland, herbaceous wetland, moss, and lichen classes into Dense Vegetation. Herbaceous Vegetation and Cropland classes were included in Sparse Vegetation, while Built-up Areas represented the Built-up class. Water bodies encompass the Snow and Ice and Permanent Water Bodies classes, and the Bare/sparse Vegetation class falls under the category of Other. Additional information on the Copernicus Global Land Cover can be found in the User Manual [61].

3. Results

3.1. Algorithm Validation

Initially, we calculated the land cover classification for the year 2023 (Figure 4), employing RF and CART algorithms along with Landsat 9 imagery. The precision results revealed that RF exhibited superior performance in terms of OA (0.95) and Kappa coefficient (0.93), whereas CART yielded lower values (OA of 0.93 and Kappa coefficient of 0.89). Consequently, we opted to proceed with subsequent analyses exclusively utilising the RF algorithm.

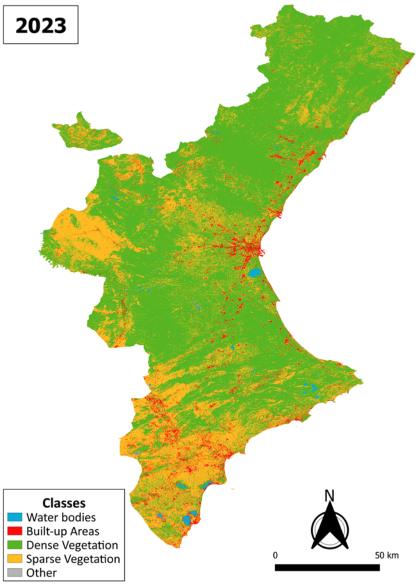

Figure 4. Land cover classification for the validation obtained with the Random Forest algorithm, using Landsat 9 images collected during September and October 2023.

Afterwards, the result obtained with the RF algorithm was validated with in situ data. In Figure 5, the confusion matrix obtained is represented. The validation results demonstrate an OA of 0.88 and a Kappa coefficient of 0.81. Noteworthy are the producer and consumer accuracies, denoting the fidelity of predictions to actual instances, which stand at 0.89 and 0.88, respectively.

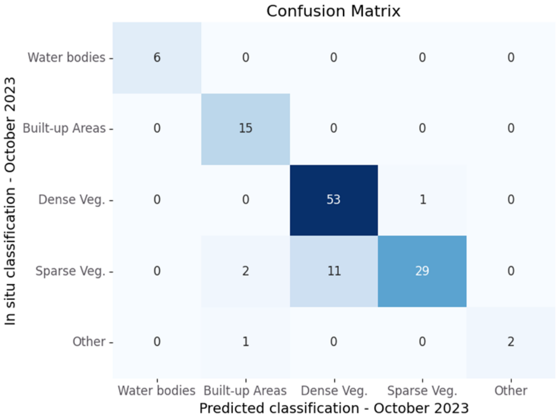

Figure 5. Confusion matrix of the 2023 land cover map calculated with Random Forest algorithm and in situ data, gathered on the 30 and 31 of October, 2023.

3.2. Land Cover Temporal Analysis

After model validation, a temporal analysis of land cover change in the Valencian Community was conducted utilising Landsat 5–9 imagery spanning the period from 1984 to 2022. All classification maps obtained can be referenced in Appendix A. Figure 6 provides a zoomed-in depiction of the city of Valencia, showcasing the classification maps derived from Landsat 5 in 1984 and Landsat 9 in 2022, respectively.

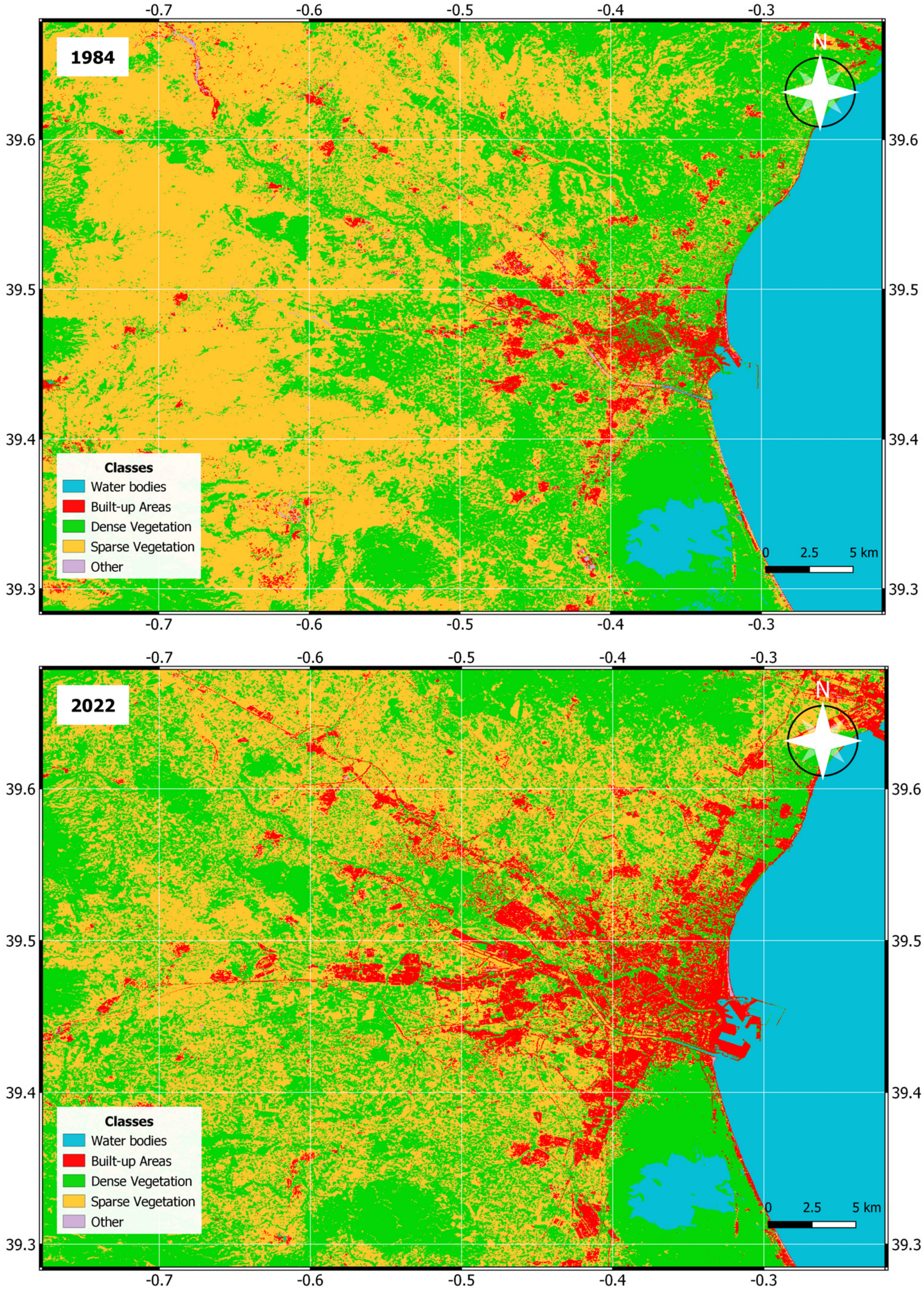

Figure 6. Land cover classifications of Valencia region obtained with the Random Forest algorithm for the years 1984 (**top**) and 2022 (**bottom**) using Landsat 5 and Landsat 9 images, respectively.

A notable surge in the urbanised surface area (Built-up Areas class) over the designated period is evident (Table 2). Specifically, there has been a substantial increase from 481.96 km^2 to 939.40 km^2, indicating a remarkable 94.9% growth for this particular class. This urban expansion has impacted green and cultivated regions (Dense and Sparse Vegetation classes), resulting in a cumulative reduction equivalent to 1.5% of the total area recorded in 1984, transitioning from 22,525.07 km^2 to 22,179.86 km^2. Solely in the Built-up Areas class, there has been an increase of 457.44 km^2, roughly equivalent to 64,000 football fields, signifying a substantial amount of urban expansion.

Table 2. Area for each class (in km^2) obtained using the Random Forest algorithm for the years 1984 and 2022, along with the corresponding percentage change within this timeframe.

Class	Area (km^2)		Percentage Change (%)
	1984	2022	1984 → 2022
Water bodies	93.57	103.75	+10.8
Built-up Areas	481.96	939.40	+94.9
Dense Vegetation	10,879.22	13,938.30	+28.1
Sparse Vegetation	11,645.85	8241.56	−29.3
Other	154.78	32.86	−78.8

Conversely, the Water Bodies class showed only a slight increase, while the Other class experienced a significant decline, decreasing by 78.8%. This reduction is also attributed to urban expansion.

The RF algorithm was systematically applied at five-year intervals throughout the study period (the resulting land covers can be found in Appendix A). This approach facilitated a comprehensive analysis of temporal changes in land cover classes, aiding in the identification of potential trends. Figure 7 visually illustrates these temporal evolutions, graphically depicting the percentage of area occupied by each class referred to as the total area of the Valencian Community.

In the case of the Built-up Areas class, a discernible and consistent growth pattern is evident, increasing from 2.08% in 1985 to 3.91% in 2020 (Tables 3 and 4). Conversely, other classes do not exhibit a clear growth or decline trajectory. Notably, the combined areas of Dense and Sparse Vegetation classes remain relatively constant, indicating an inversely proportional relationship between the two classes. This observation aligns with the annual variations in crop density during the summer season, as well as with the variations in overall vegetation density and intensity. Figure 8 presents a composite graph where the percentages occupied by all classes are collectively represented for each year. In the majority of instances, Dense Vegetation emerges as the predominant class, occupying the highest percentage.

Table 3. Area (km^2) of each class obtained with the Random Forest algorithm, calculated every 5 years using Landsat 5–8 images for the period 1985–2020.

Class	1985	1990	1995	2000	2005	2010	2015	2020
Water bodies	87.82	116.61	82.13	88.06	87.38	111.98	125.19	116.70
Built-up Areas	484.24	702.85	759.72	788.41	849.70	857.32	869.84	908.57
Dense Veg.	11,212.25	14,060.05	10,460.70	13,150.16	12,159.99	13,934.87	12,631.18	14,437.68
Sparse Veg.	11,324.52	8237.74	11,780.41	9159.91	10,038.23	8318.86	9571.46	7762.19
Other	146.59	138.36	171.92	68.85	120.02	32.59	57.81	30.70

Table 4. Area (%, referring to the total area of the Valencian Community) of each class obtained with the Random Forest algorithm, calculated every 5 years using Landsat 5–8 images, for the period 1985–2020.

Class	1985	1990	1995	2000	2005	2010	2015	2020
Water bodies	0.38	0.50	0.35	0.38	0.38	0.48	0.54	0.50
Built-up Areas	2.08	3.02	3.27	3.39	3.65	3.69	3.74	3.91
Dense Veg.	48.21	60.46	44.98	56.55	52.29	59.92	54.31	62.08
Sparse Veg.	48.70	35.42	50.66	39.39	43.17	35.77	41.16	33.38
Other	0.63	0.59	0.74	0.30	0.52	0.14	0.25	0.13

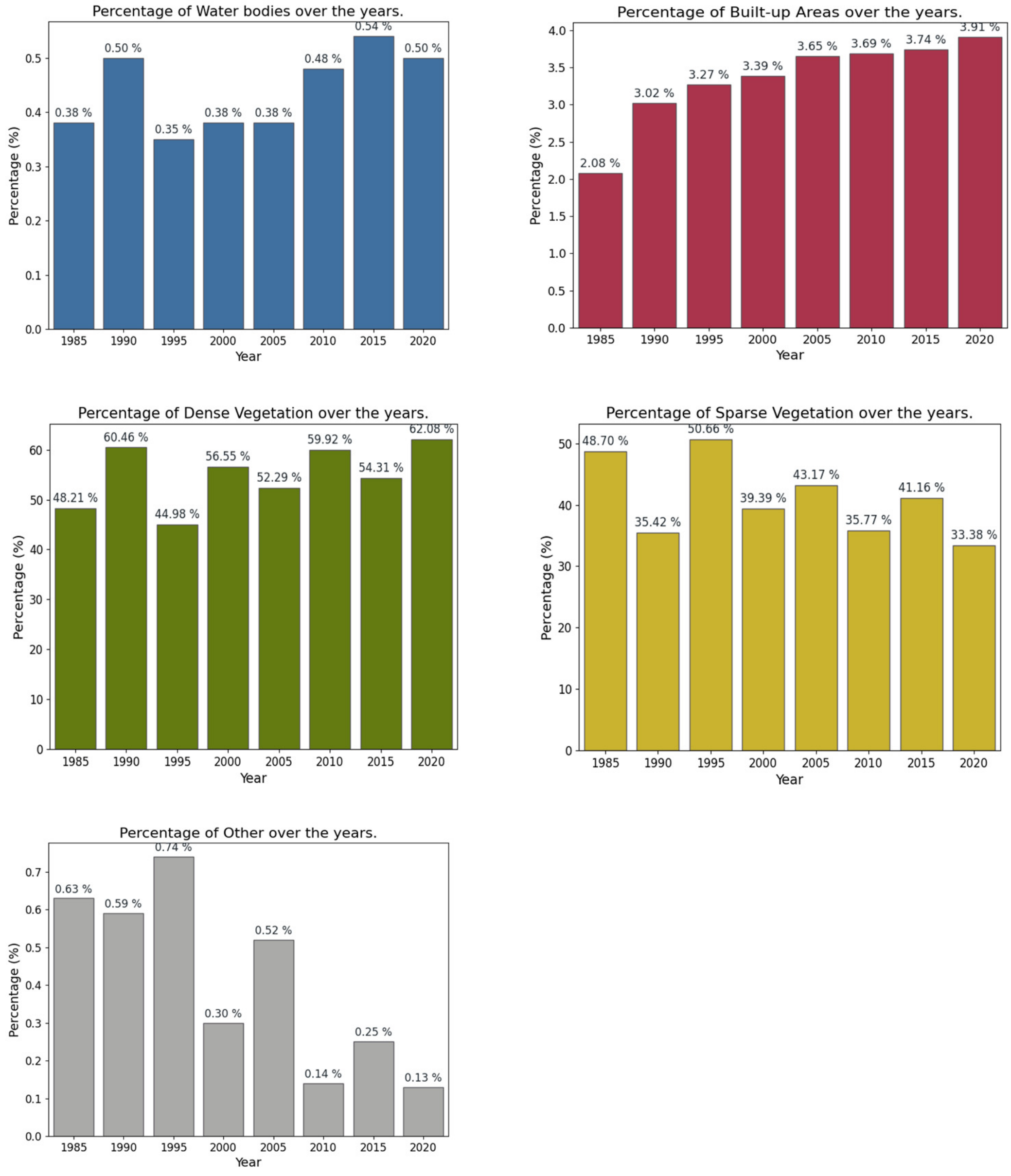

Figure 7. Graph illustrating the percentage distribution of land cover classes in the Valencian Community. The calculations were performed every 5 years using Landsat 5–8 images, covering the period from 1985 to 2020.

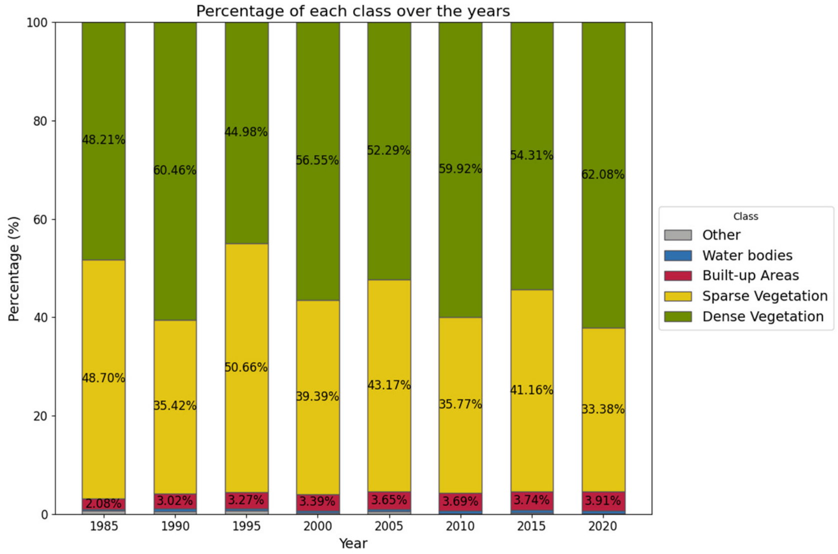

Figure 8. Graph illustrating the overall percentage distribution of land cover classes in the Valencian Community. The calculations were performed every 5 years using Landsat 5–8 images, covering the period from 1985 to 2020.

Subsequently, linear and polynomial adjustments were employed to examine trends for each class from 1984 to 2022. The consistent growth in the Built-up Areas class and the simultaneous decline in the combined Dense and Sparse Vegetation classes reveal a positive trend indicative of urban expansion in the community. Conversely, a negative trend signals an overall reduction in vegetation (Figure 9). In both cases, polynomial regression yields the best fit (R^2 of 0.95 and 0.84 for Built-up Areas and Sparse + Dense Vegetation, respectively). The 'Water bodies' class shows no clear trend, maintaining oscillations between similar values throughout the period.

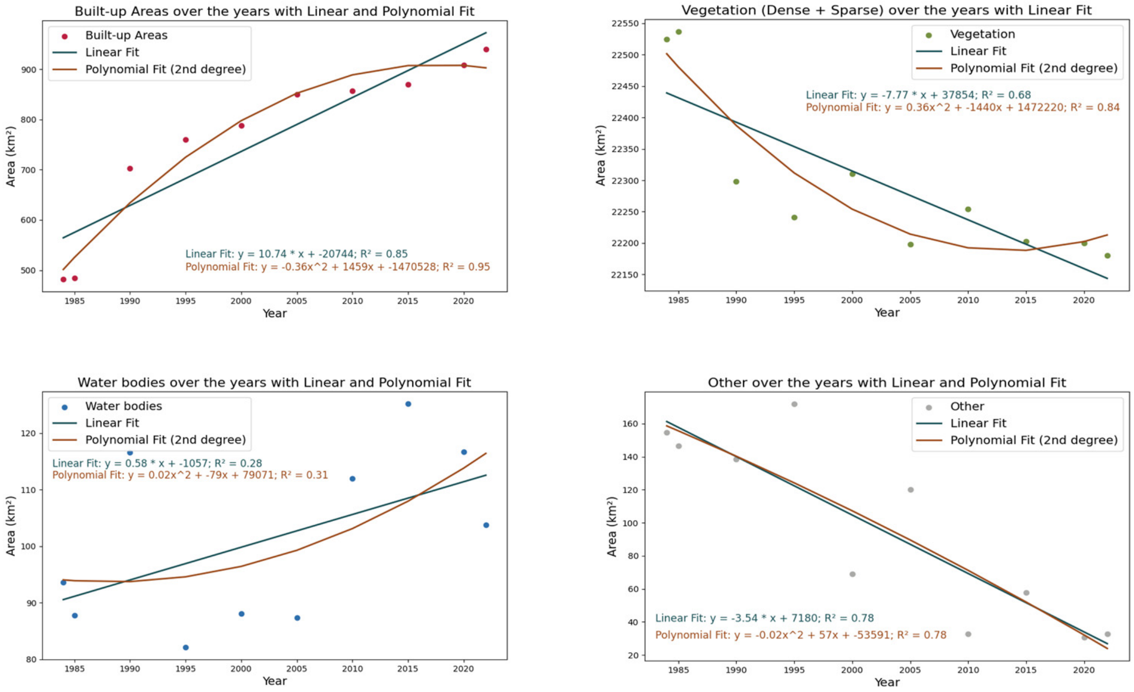

Figure 9. Polynomial regression performed in the Built-up Areas class (**top left**), Dense + Sparse Vegetation (**top right**), Water Bodies (**bottom left**), and Other (**bottom right**), spanning the period from 1984 to 2022.

A separate analysis of both Dense and Sparse Vegetation classes reveals consistent fluctuations over the years. Some years, such as 1990 (60.46%) and 2020 (62.08%), show high percentages of Dense Vegetation, while others, including 1985, 1995, and 2005, show lower percentages (48.21%, 44.98%, and 54.31%, respectively).

Concerning the 'Other' class, it manifests a negative trend (R^2 of 0.78).

In Figure 10, a superimposition of the Built-up Areas classes for all years, each represented by a distinct colour, facilitates the observation of urban growth in the cities of Valencia, Alicante, and Castellón throughout the study interval. We can observe that the most significant urbanisation impact occurred from 1985 to 1990, as previously discussed. Additionally, the introduction of ports in 2005 (absent in 2000) and their subsequent expansions in 2010, 2015, and 2020 are discernible.

Analysing the percentage of 'Built-up Areas' in 2020 of these regions, we observed a rise of 110.37% (an additional 56.59 km^2) in Castellón, a 70.47% increase (adding 143.30 km^2) in Valencia, and a remarkable growth of 157.68% (an addition of 100.20 km^2) in Alicante, compared to 1985 (Figure 11), revealing a significant increase over these 35 years.

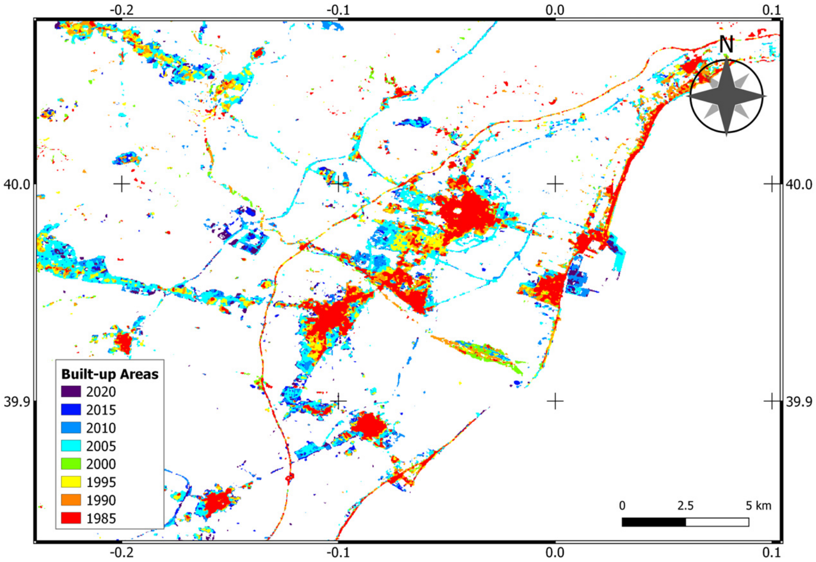

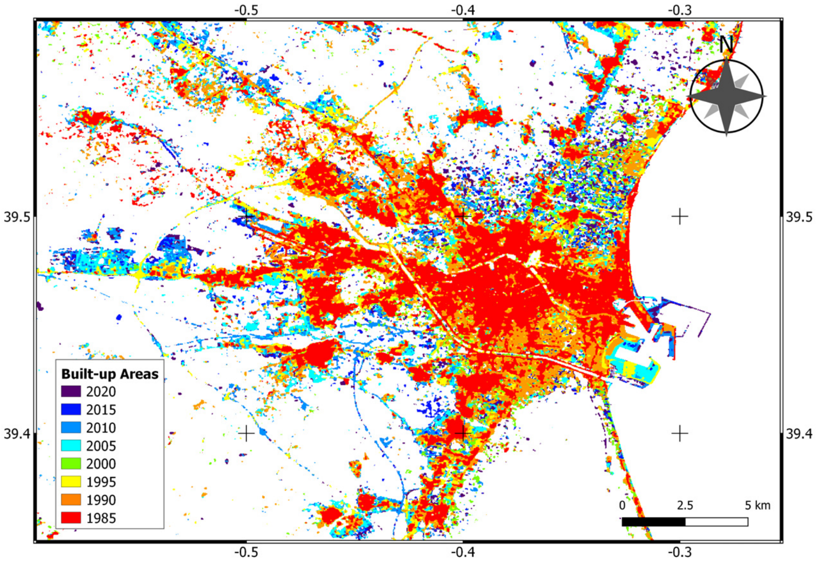

Figure 10. *Cont.*

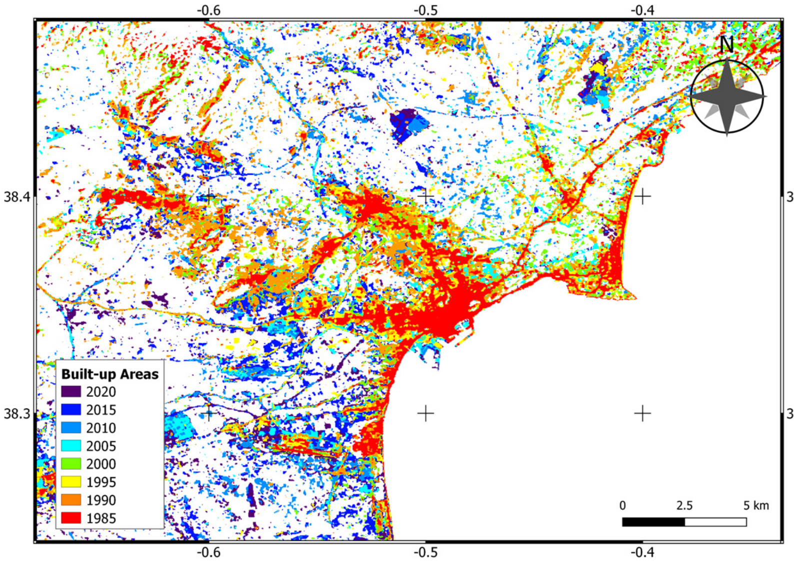

Figure 10. Maps illustrating the expansion of Built-up Areas class in Castellón (**top**), Valencia (**centre**), and Alicante (**bottom**) for the period 1985–2020.

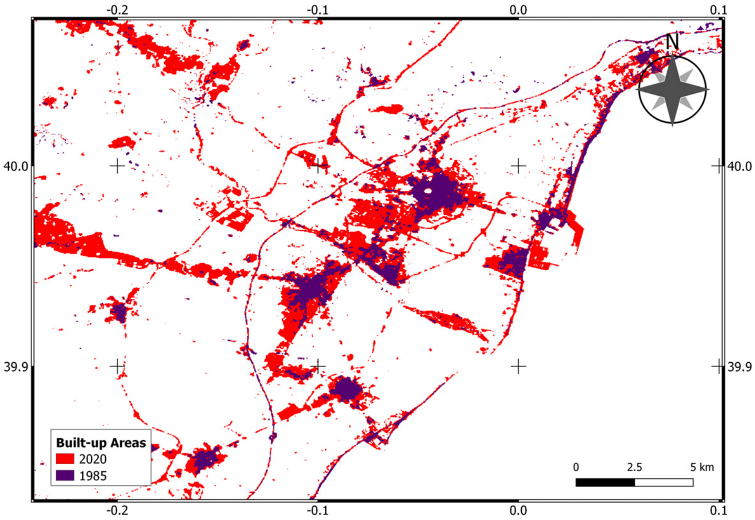

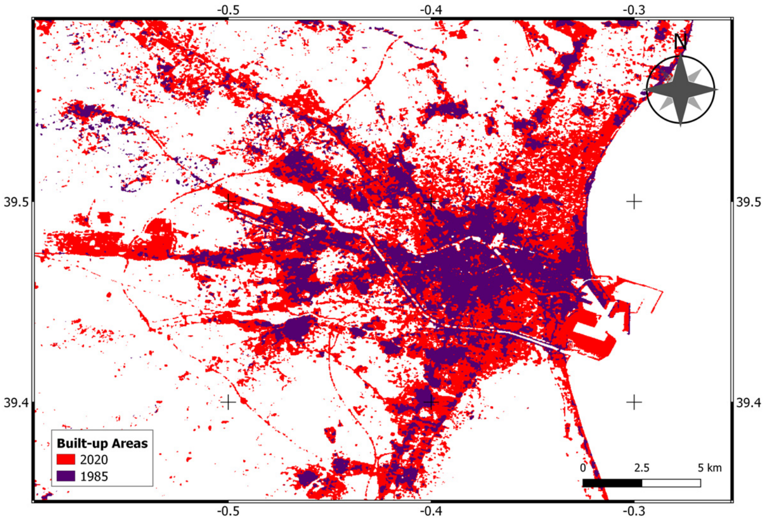

Figure 11. *Cont.*

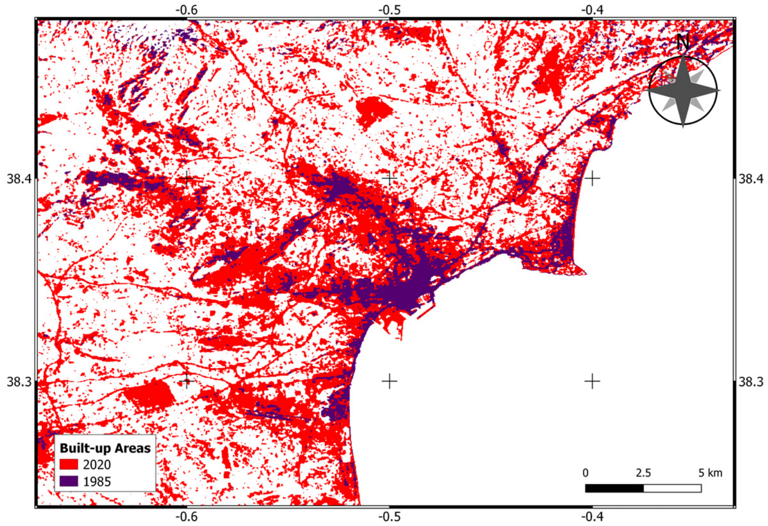

Figure 11. Maps illustrating the expansion of Built-up Areas class in Castellón (**top**), Valencia (**centre**), and Alicante (**bottom**) between 1985 and 2020. The Built-up Areas class shows a rise of 110.37% (an additional 56.59 km^2) in Castellón, a 70.47% increase (adding 143.30 km^2) in Valencia, and a remarkable growth of 157.68% (an addition of 100.20 km^2) in Alicante.

3.3. Holdout Validation

Holdout Validation was performed for each of the calculated land covers. This approach, involving the partitioning of data into training and testing sets, has been crucial for assessing and ensuring the effectiveness of our model across various years. Table 5 presents the OA and Kappa coefficients for each year. Remarkably, OA ranges from 92% to 95%, and the Kappa coefficient varies between 89% and 92%.

Table 5. OA and Kappa coefficient results of the Holdout Validation for each year. The validation was performed while allocating 70% of the dataset for training and reserving 30% for testing purposes.

	1984	**1985**	**1990**	**1995**	**2000**	**2005**	**2010**	**2015**	**2020**	**2022**
Overall Accuracy (%)	94.16	93.85	91.72	93.37	92.18	92.96	94.52	95.02	94.90	94.81
Kappa (%)	90.67	90.03	87.54	89.48	87.13	89.03	90.79	91.90	90.78	91.79

3.4. Comparison with Copernicus Global Land Cover and ESA WorldCover

An additional method used to validate our land cover products involves their comparison with other datasets, such as the 2015 Copernicus Global Land Cover and the 2020 WorldCover by ESA (Figure 12). The comparison was conducted on a pixel-by-pixel basis, scrutinising all pixels within the Valencian Community. In the case of the comparison with Copernicus' product, our classification was initially rescaled to the same resolution of Copernicus Global Land Cover (100 m), and then the classes from Copernicus matching of those created by us were selected to generate a confusion matrix (Figure 13).

This comparison revealed a significant number of points where Copernicus classifies areas as urban, which in our classification belong to Sparse and Dense Vegetation. Furthermore, the multitude of vegetation classes in Copernicus results in our Sparse Vegetation values corresponding to different classes defined by them, although Dense Vegetation aligns for the most part. In this case, the percentage of urban area corresponds to 6.91%, slightly higher than the value obtained in our land cover (3.74%), attributable to the factors discussed earlier.

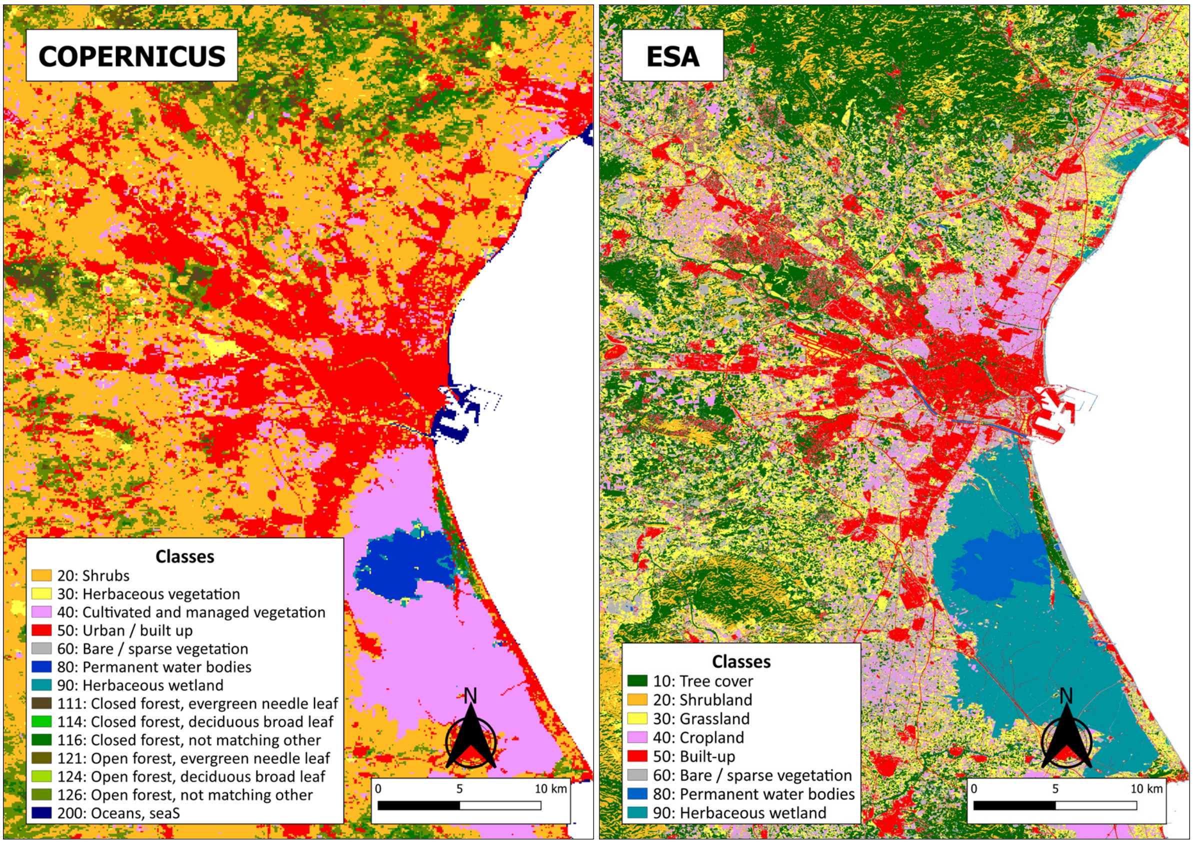

Figure 12. Global Land Cover provided by Copernicus for the year 2015 (**left**) and WorldCover v100 2020 provided by ESA (**right**).

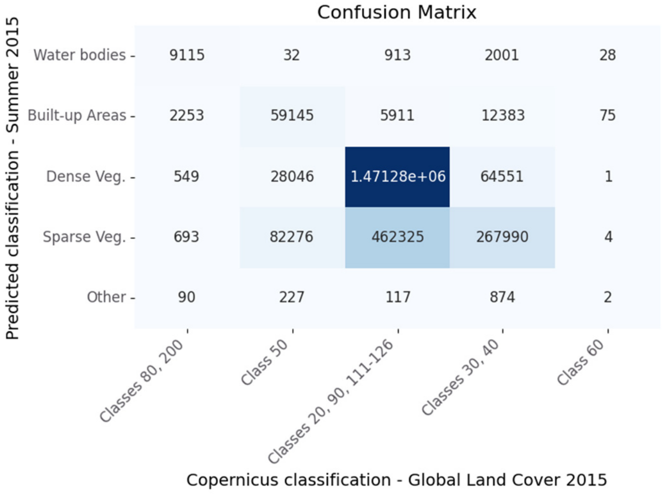

Figure 13. Confusion matrix comparing the 2023 land cover map calculated with the Random Forest algorithm and the one provided by Copernicus. Classes 80 and 200 correspond to Water Bodies class; class 50 represents Built-up Areas class; classes 20, 90, and 111–126 pertain to Dense Vegetation; classes 30 and 40 represent Sparse Vegetation; and class 60 represents the Other class.

The OA achieved was 0.73, accompanied by a Kappa coefficient of 0.41 and producer and consumer accuracies of 0.75 and 0.73, respectively.

Regarding the WorldCover provided by ESA, it was rescaled from the original resolution of 10 m to match the resolution of our product (30 m). The WorldCover comprises multiple classes (Figure 12), which were grouped according to their closest resemblance to ours. The confusion matrix obtained through the pixel-by-pixel comparison (Figure 14) suggests that the ESA urban class sometimes corresponds to our vegetation pixels. This response, similar to that obtained for the Copernicus product, possibly has similar reasons. It is worth noting that no class equivalent to our Other class was identified in WorldCover. This discrepancy arises from their inclusion of bare soil within the Sparse Vegetation class, leading most of our points in the Other class to be categorised as vegetation classes in WorldCover. In this instance, the urban area percentage is 4.31%, more closely aligning with the value obtained in our land cover (3.91%).

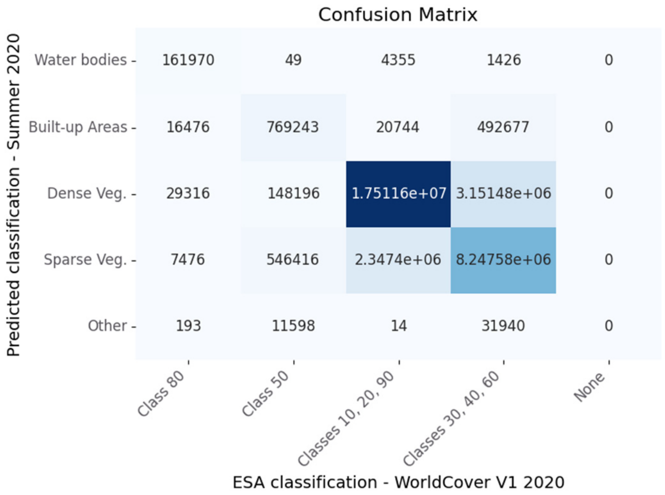

Figure 14. Confusion matrix of the 2023 land cover map calculated with Random Forest algorithm and the one provided by ESA. Class 80 corresponds to Water Bodies class; class 50 represents Built-up Areas class; classes 10, 20 and 90 pertain to Dense Vegetation; classes 30, 40, and 60 indicate Sparse Vegetation; and None represents the Other class.

For our vegetation classes, a substantial alignment is observed with the various classes they define. However, the presence of multiple classes results in some points of Dense Vegetation corresponding to what we grouped as Sparse Vegetation and vice versa. Consequently, an OA of 0.80, a Kappa coefficient of 0.60, and producer and consumer accuracies of 0.80 each were obtained.

4. Discussion

Regarding the validation of the algorithm, the confusion matrix (Figure 5) reveals a generally accurate reflection of real land cover. There is an exception in the classification of sparse vegetation, occasionally misidentified as dense vegetation. This discrepancy may arise from the challenge of precisely assessing vegetation density from ground-level perspectives, where the angle of vision varies, making it difficult to discern the intensity/density of vegetation. However, it is important to highlight that the classification consistently identifies these areas as vegetation, mitigating the impact of the error. It is worth remembering that mapping extensive areas in complex landscapes proves challenging due to abrupt changes in environmental gradients such as humidity, altitude, and temperature. These diverse landscapes exhibit land cover categories that are challenging to differentiate spectrally, given the low separability between classes and high intra-class variability [24].

Anyway, the metrics obtained collectively affirm the robust performance of the RF model, characterised by a commendable classification accuracy and a substantial concordance between predictions and ground truth values.

Moving on to the analysis of change at a temporal level, the steady growth of the Built-up Areas class can be attributed to significant urban expansion during the 1980s/1990s, which has continued, albeit to a lesser extent over the decades, leading to a corresponding decline in vegetation.

The oscillation in the ratio between Dense and Sparse Vegetation is attributed to annual variations in the rainfall regime, which influence plant growth, and to shifts in crop types, resulting in alternating vegetation patterns. The years 1990 and 2020, identified by the national Spanish meteorological agency (Agencia Estatal de Meteorologia, AEMET) as concluding years of periods marked by substantial rainfall, exhibit the highest percentages of Dense Vegetation. In contrast, the years 1985, 1995, and 2005, corresponding to periods of pronounced aridity, display lower percentages of Dense Vegetation and higher proportions of Sparse Vegetation. This pattern underscores the impact of reduced precipitation during these years, contributing to diminished plant growth and a shift toward a prevalence of less densely vegetated areas.

Finally, the decline in the Other class indicates that areas previously classified as bare soil, beaches, etc., have likely undergone urbanisation and now form part of Built-up Areas.

Analysing the land covers in greater detail (Figure 10), it is notable how urban expansion in rural areas began around the years 2000/2005, while the most substantial city expansion occurred from 1985 to 1990. Numerous areas classified as non-urban in 1985 began urbanised zones over the subsequent years. These regions, initially characterised as rural landscapes, have undergone substantial development, evolving into small towns or cities. The spatial distribution highlights the concentration of increased urbanisation along key transportation arteries and adjoining the pre-established urban core. These transformations underscore the dynamic and evolving nature of land cover in the Valencian Community, portraying the intricate interplay between urban expansion and the transformation of rural landscapes.

The validation process emphasised the accuracy and precision of the maps produced. In particular, the high OA and Kappa values of the holdout validation demonstrate the strength and reliability of the data. Regarding the comparison with the Copernicus Global Land Cover and the WorldCover by ESA, the results indicate reasonable agreement between the three land covers, albeit with a somewhat low Kappa coefficient attributed to some discrepancies.

These discrepancies may arise from the higher resolution of our product, allowing for the differentiation of various urban cores within cities and the recognition of different vegetation types in between, while the other products represent cities as a single compact urban area, as can be noticed in Figure 12. Furthermore, the non-exact correspondence of the classes used in the different land covers certainly has an effect on the inaccuracy of the comparison.

Finally, it is noteworthy that both the Copernicus Global Land Cover and the ESA WorldCover utilize products from throughout the year to derive the final land cover. In contrast, our study has focused solely on the summer of each year. This distinction in temporal scope may contribute to differences observed between the land covers, as seasonal variations can affect land cover characteristics.

Considering these differences, we believe that the results obtained are reliable, and we are satisfied with the accuracy achieved.

5. Conclusions

In this study, we conducted a comprehensive analysis of land cover dynamics in the Valencian Community, spanning from 1984 to 2023. Employing advanced algorithms, specifically RF and CART, we initially classified the land cover for the year 2023 using Landsat 9 imagery. The accuracy test results favoured RF, demonstrating superior OA (0.95) and Kappa coefficient (0.93) compared to CART. The subsequent validation process with in situ data highlighted the model's generally accurate reflection of real land cover, notwithstanding occasional misclassifications, particularly in Sparse Vegetation. This discrepancy was attributed to challenges in precisely assessing the vegetation density from ground-level perspectives, mitigated by the consistent identification of these areas as vegetation. Moreover, mapping extensive areas in complex landscapes proved challenging due to environmental gradients influencing spectral differentiability. Subsequent temporal analysis revealed a notable surge in urbanised surface area, affecting vegetation classes. Notably, the Built-up Areas class exhibited a substantial 95% increase from 1984 to 2022, displaying consistent urban expansion trends. Linear and polynomial adjustments further affirmed this growth pattern, with the Built-up Areas class demonstrating a polynomial regression fit (R^2 of 0.95).

Regarding the other land cover classes, Water Bodies maintained relative stability, exhibiting minor fluctuations. Conversely, Dense and Sparse Vegetation classes collectively witnessed a cumulative decrease of 1.5% from 1984, indicative of the encroachment of urban areas over the years. Further analysis of the Other class unveiled a significant negative trend, underscoring the influence of urbanisation on areas once classified as bare soil and beaches.

Holdout Validation, a pivotal step in assessing model performance, consistently showcased high accuracy, with OA ranging from 92% to 95% and Kappa coefficients between 89% and 92%. This method, involving data partitioning into training and testing sets, ensured the reliability and effectiveness of our model across diverse years.

A comparison with external land covers revealed reasonable agreement, albeit with some discrepancies attributed to resolution differences and class definitions. The study's temporal focus on summer versus the yearly coverage of external products contributed to the observed variations.

These findings not only elucidate the tangible consequences of urban growth in the Valencian Community but also offer valuable insights into broader environmental implications. The pronounced evolution from non-urban to urbanised areas over the years emphasises the transformative impact of human activities on the regional landscape.

This dynamic urbanisation, as depicted in the land cover analysis, has implications beyond immediate spatial changes. In recent years, numerous studies have demonstrated the relationship between increased urban temperatures and specific surfaces or the lack of vegetation, among other factors [62]. Having a detailed classification map and correlating it with temperature maps, for instance, would allow for the development of mitigation strategies. These strategies could include the implementation of green spaces, thereby reducing urban temperatures and mitigating the Urban Heat Island effect. Such integrative approaches are crucial for creating sustainable and liveable urban environments [63,64].

Moreover, this comprehensive view of land cover dynamics within the Valencian Community provides a valuable tool for anticipating and managing environmental challenges. The interplay between urbanisation, land cover changes, and environmental impacts underscores the need for sustainable urban planning and environmental management strategies. As urban areas continue to evolve, these insights become crucial for informed decision making, contributing to a more resilient and ecologically balanced future for the region.

Author Contributions: The conceptualisation, project administration, and funding acquisition were spearheaded by J.A.S., while V.C. and S.G. handled data curation and methodology. The validation process and the initial drafting of the manuscript were collaboratively conducted by V.C., S.G. and Á.S.-G. All authors have read and agreed to the published version of the manuscript.

Funding: This research was funded by the European Union and Valencian Community, who co-financed the project 'Estimación de Indicadores Medioambientales en la Comunidad VALENciana usando datos de SATélite (VALENSAT)', part of INVESTIGO 2022 financing plan (INVEST/2022/411), and by the Ministerio de Ciencia e Innovación PID2020-112494RB-I00 IPL-LSTM.

Data Availability Statement: Data are contained within the article.

Acknowledgments: We are sincerely grateful to the European Space Agency (ESA) and the Copernicus program for the supply of images and validation products, which significantly contributed to the research efforts presented in this paper. We acknowledge Google Earth Engine for its indispensable data-processing capabilities, which greatly facilitated the handling of the substantial volume of data utilised in this study.

Conflicts of Interest: The authors declare no conflicts of interest. The funders had no role in the design of the study; in the collection, analyses, or interpretation of data; in the writing of the manuscript; or in the decision to publish the results.

Appendix A

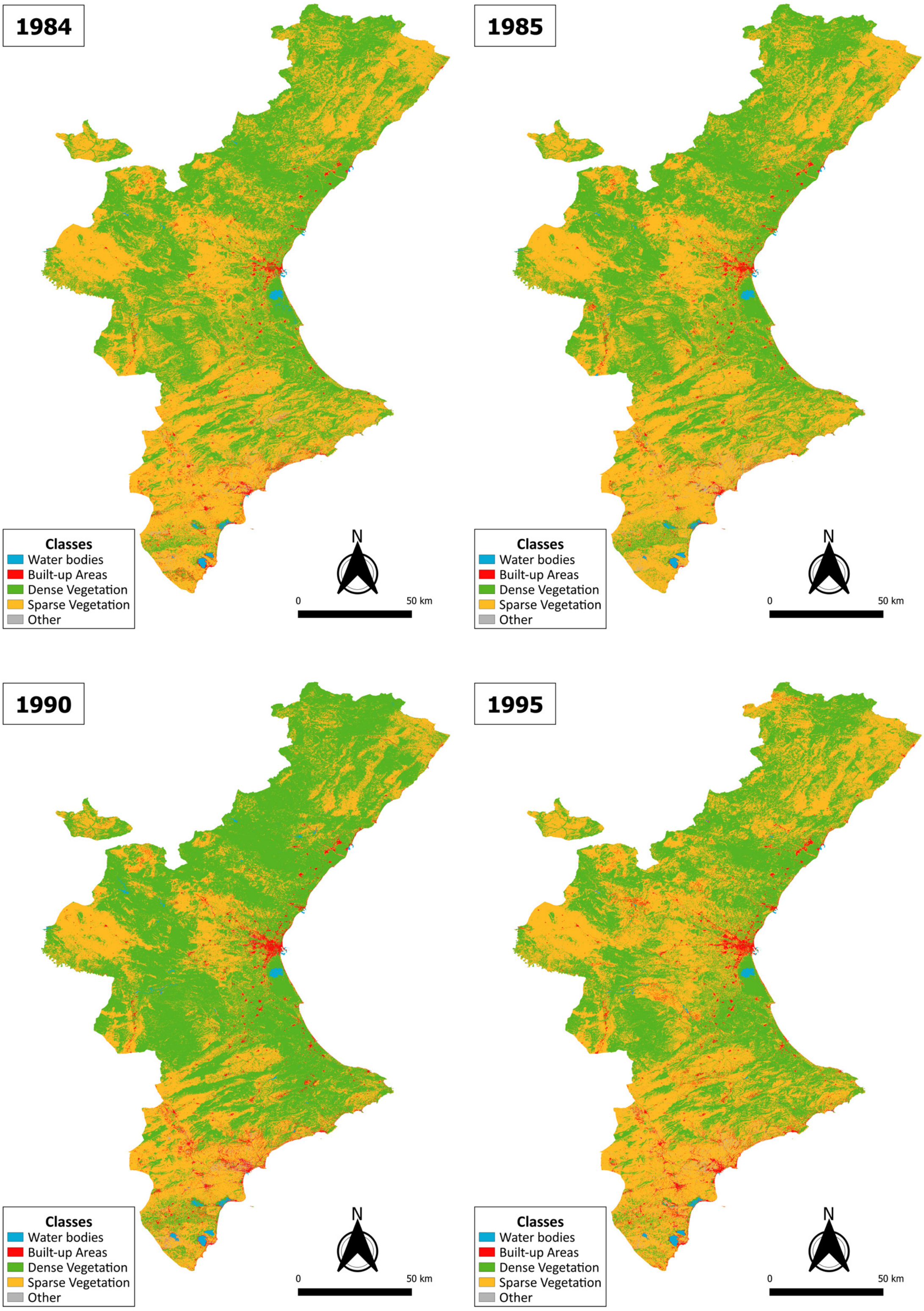

Figure A1. *Cont.*

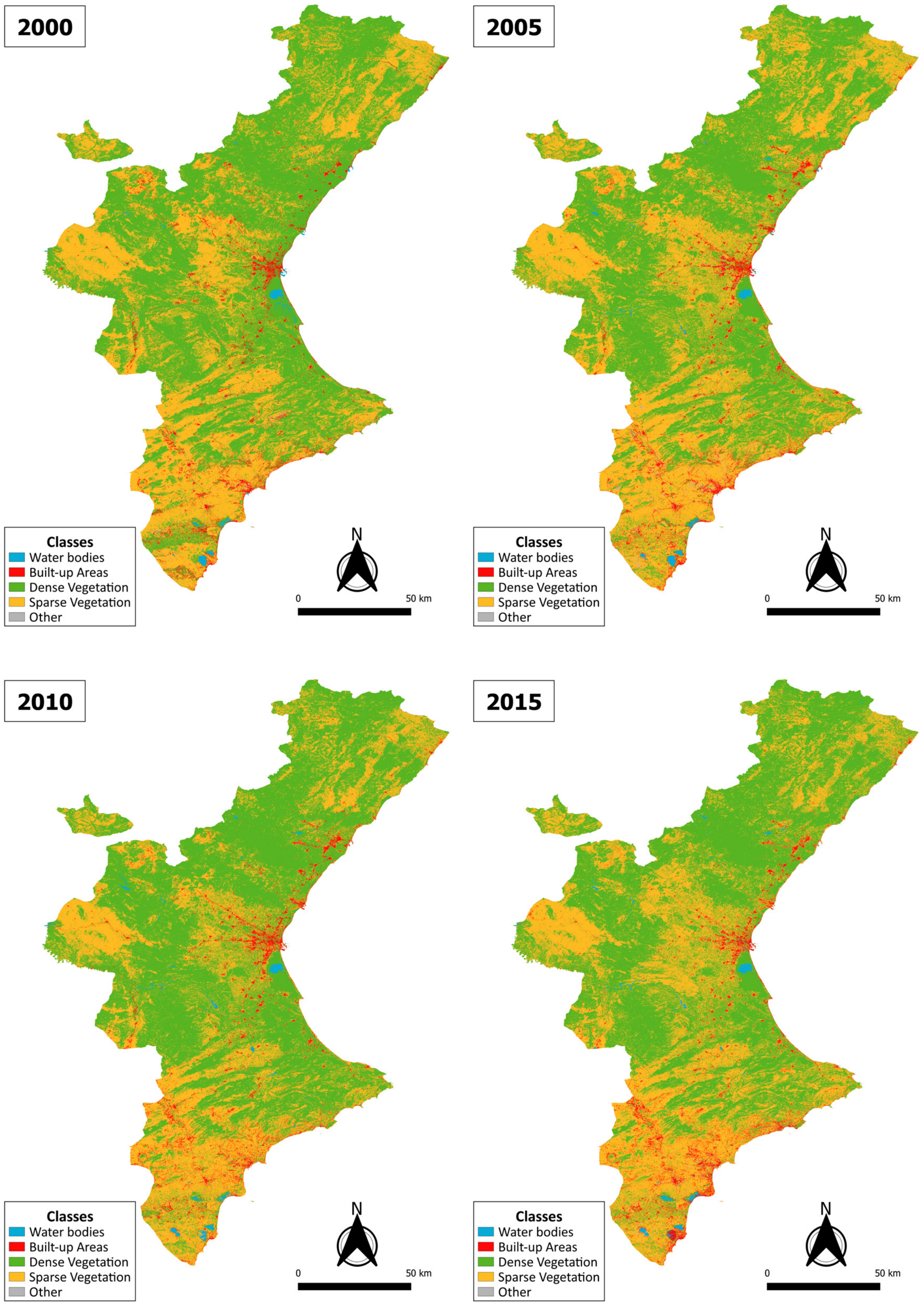

Figure A1. *Cont.*

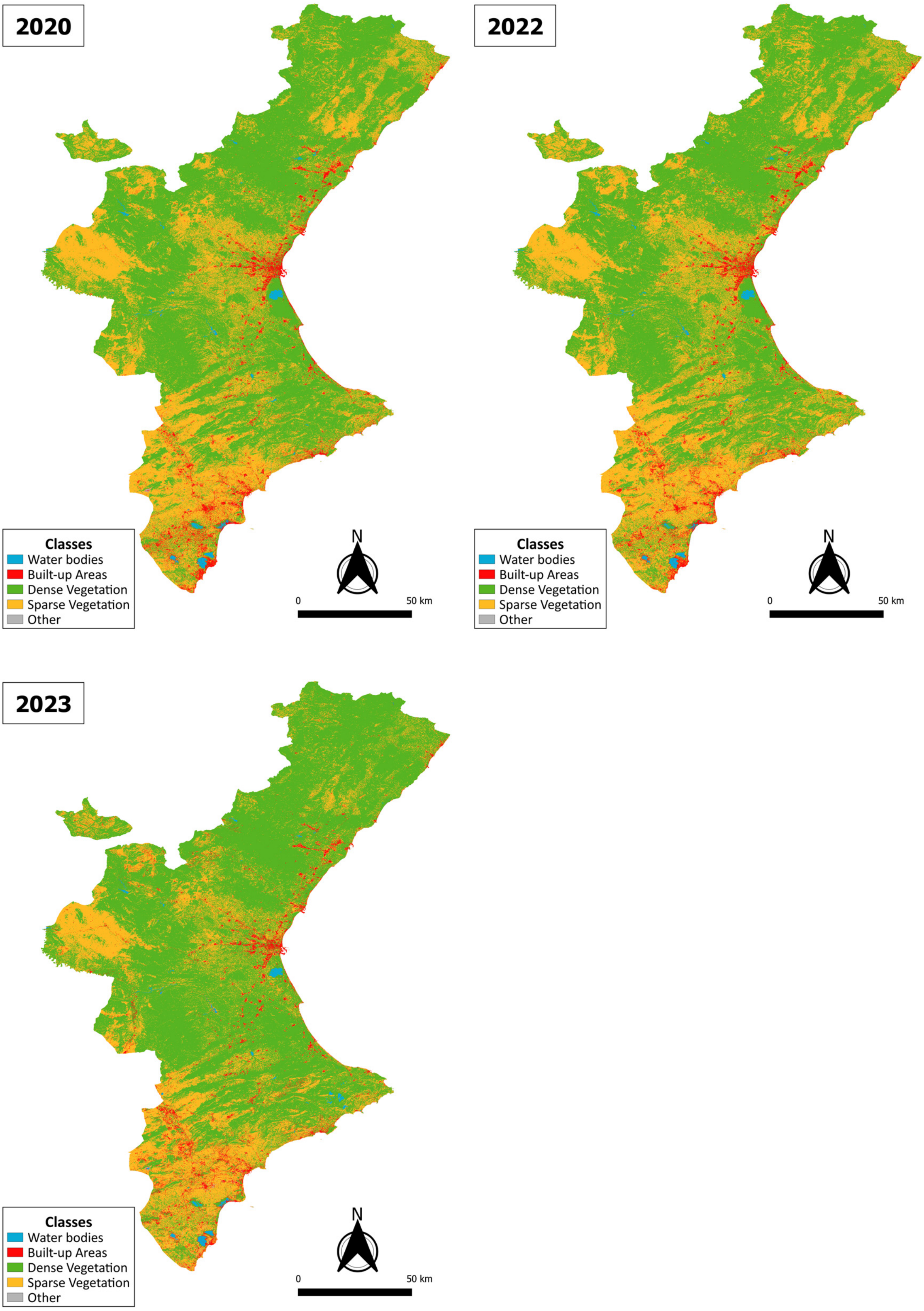

Figure A1. Land cover classification obtained with the Random Forest algorithm, using Landsat 5–9 imagery for the period 1984–2023.

References

1. Hashem, N.; Balakrishnan, P. Change analysis of land use/land cover and modelling urban growth in Greater Doha, Qatar. *Ann. GIS* **2014**, *21*, 233–247. [CrossRef]
2. Turner, B.L.; Lambin É, F.; Reenberg, A. The emergence of land change science for global environmental change and sustainability. *Proc. Natl. Acad. Sci. USA* **2007**, *104*, 20666–20671. [CrossRef] [PubMed]
3. Brovkin, V.; Sitch, S.; Von Bloh, W.; Claußen, M.; Bauer, E.; Crämer, W. Role of land cover changes for atmospheric CO_2 increase and climate change during the last 150 years. *Glob. Chang. Biol.* **2004**, *10*, 1253–1266. [CrossRef]
4. Dutta, D.; Rahman, A.; Paul, S.K.; Kundu, A. Changing pattern of urban landscape and its effect on land surface temperature in and around Delhi. *Environ. Monit. Assess.* **2019**, *191*, 551. [CrossRef] [PubMed]
5. Liou, Y.; Kar, S.; Chang, L. Use of high-resolution FORMOSAT-2 satellite images for post-earthquake disaster assessment: A study following the 12 May 2008 Wenchuan earthquake. *Int. J. Remote Sens.* **2010**, *31*, 3355–3368. [CrossRef]
6. Nguyen, K.A.; Liou, Y.A.; Tran, H.P.; Hoang, P.P.; Nguyễn, T.H. Soil salinity assessment by using near-infrared channel and vegetation soil salinity index derived from LaNDSAt 8 OLI data: A case study in the Tra Vinh province, Mekong Delta, Vietnam. *Prog. Earth Planet. Sci.* **2020**, *7*, 1. [CrossRef]
7. Mas, J.; Lemoine-Rodríguez, R.; González-López, R.; López-Sánchez, J.G.; Piña-Garduño, A.; Herrera-Flores, E. Land use/land cover change detection combining automatic processing and visual interpretation. *Eur. J. Remote Sens.* **2017**, *50*, 626–635. [CrossRef]
8. Sterling, S.; Ducharne, A.; Polcher, J. The impact of global land-cover change on the terrestrial water cycle. *Nat. Clim. Chang.* **2012**, *3*, 385–390. [CrossRef]
9. Salazar, Á.; Baldi, G.; Hirota, M.; Syktus, J.; McAlpine, C. Land use and land cover change impacts on the regional climate of non-Amazonian South America: A review. *Glob. Planet. Chang.* **2015**, *128*, 103–119. [CrossRef]
10. Talukdar, S.; Singha, P.; Shahfahad Mahato, S.; Praveen, B.; Rahman, A. Dynamics of Ecosystem Services (ESS) in response to Land use Land cover (LU/LC) changes in the Lower Gangetic Plain of India. *Ecol. Indic.* **2020**, *112*, 106121. [CrossRef]
11. Liou, Y.A.; Nguyen AT, N.; Li, M.H. Assessing spatiotemporal eco-environmental vulnerability by Landsat data. *Ecol. Indic.* **2017**, *80*, 52–65. [CrossRef]
12. Chen, Z.; Wang, L.; Wei, A.; Gao, J.; Li, Y.; Zhou, J. Land-use change from arable lands to orchards reduced soil erosion and increased nutrient loss in a small catchment. *Sci. Total Environ.* **2019**, *648*, 1097–1104. [CrossRef]
13. Hemati, M.; Hasanlou, M.; Mahdianpari, M.; Mohammadimanesh, F. A Systematic Review of LanDsAt Data for Change Detection Applications: 50 years of Monitoring the Earth. *Remote Sens.* **2021**, *13*, 2869. [CrossRef]
14. Hoffmann, J. The future of satellite remote sensing in hydrogeology. *Hydrogeol. J.* **2005**, *13*, 247–250. [CrossRef]
15. Gómez, C.; White, J.C.; Wulder, M.A. Optical Remotely Sensed Time Series Data for land Cover Classification: A review. *ISPRS J. Photogramm. Remote Sens.* **2016**, *116*, 55–72. [CrossRef]
16. Chuvieco, E. *Fundamentals of Satellite Remote Sensing*; CRC Press eBooks: Boca Raton, FL, USA, 2020. [CrossRef]
17. Ghimire, B.; Rogan, J.; Galiano, V.R.; Panday, P.K.; Neeti, N. An evaluation of bagging, boosting, and random forests for Land-Cover classification in Cape Cod, Massachusetts, USA. *Gisci. Remote Sens.* **2012**, *49*, 623–643. [CrossRef]
18. Sesnie, S.E.; Gessler, P.E.; Finegan, B.; Thessler, S. Integrating LaNdsAT TM and SRTM-DEM derived variables with decision trees for habitat classification and change detection in complex neotropical environments. *Remote Sens. Environ.* **2008**, *112*, 2145–2159. [CrossRef]
19. Kulkarni, A.D.; Lowe, B. Random Forest Algorithm for Land Cover Classification. Computer Science Faculty Publications and Presentations, 2016. Paper 1. Available online: http://hdl.handle.net/10950/341 (accessed on 26 September 2023).
20. Campos-Taberner, M.; García-Haro, F.J.; Martínez, B.; Izquierdo-Verdiguier, E.; Atzberger, C.; Camps-Valls, G.; Gilabert, M.A. Understanding deep learning in land use classification based on Sentinel-2 time series. *Sci. Rep.* **2020**, *10*, 17188. [CrossRef] [PubMed]
21. Walsh, E.; Bessardon, G.; Gleeson, E.; Ulmas, P. Using machine learning to produce a very high resolution land-cover map for Ireland. *Adv. Sci. Res.* **2021**, *18*, 65–87. [CrossRef]
22. Pal, M. Random forest classifier for remote sensing classification. *Int. J. Remote Sens.* **2005**, *26*, 217–222. [CrossRef]
23. Gislason, P.O.; Benediktsson, J.A.; Sveinsson, J.R. Random Forests for land cover Classification. *Pattern Recognit. Lett.* **2006**, *27*, 294–300. [CrossRef]
24. Rodríguez-Galiano, V.; Ghimire, B.; Rogan, J.; Chica-Olmo, M.; Rigol-Sánchez, J. An assessment of the effectiveness of a random forest classifier for land-cover classification. *ISPRS J. Photogramm. Remote Sens.* **2012**, *67*, 93–104. [CrossRef]
25. Breiman, L. Random forests. *Mach. Learn.* **2001**, *45*, 5–32. [CrossRef]
26. Cutler, D.R.; Edwards, T.C.; Beard, K.H.; Cutler, A.; Hess, K.T.; Gibson, J.; Lawler, J.J. Random forests for classification in ecology. *Ecology* **2007**, *88*, 2783–2792. [CrossRef] [PubMed]
27. Friedl, M.A.; Brodley, C.E. Decision tree classification of land cover from remotely sensed data. *Remote Sens. Environ.* **1997**, *61*, 399–409. [CrossRef]
28. DeFries, R. Multiple criteria for evaluating machine learning algorithms for land cover classification from satellite data. *Remote Sens. Environ.* **2000**, *74*, 503–515. [CrossRef]
29. Belgiu, M.; Drăguţ, L. Random Forest in Remote Sensing: A review of applications and future directions. *ISPRS J. Photogramm. Remote Sens.* **2016**, *114*, 24–31. [CrossRef]

30. Naushad, R.; Kaur, T.; Ghaderpour, E. Deep Transfer Learning for Land Use and Land Cover Classification: A Comparative study. *Sensors* **2021**, *21*, 8083. [CrossRef]
31. Phan, T.N.; Kappas, M. Comparison of random Forest, K-Nearest Neighbor, and Support vector machine classifiers for land cover classification using Sentinel-2 imagery. *Sensors* **2017**, *18*, 18. [CrossRef]
32. Gorelick, N.; Hancher, M.; Dixon, M.; Ilyushchenko, S.; Thau, D.; Moore, R. Google Earth Engine: Planetary-scale Geospatial Analysis for Everyone. *Remote Sens. Environ.* **2017**, *202*, 18–27. [CrossRef]
33. Amani, M.; Ghorbanian, A.; Ahmadi, S.A.; Kakooei, M.; Moghimi, A.; Mirmazloumi, S.M.; Moghaddam, S.H.A.; Mahdavi, S.; Ghahremanloo, M.; Parsian, S.; et al. Google Earth Engine Cloud computing platform for remote sensing big data Applications: A Comprehensive review. *IEEE J. Sel. Top. Appl. Earth Obs. Remote Sens.* **2020**, *13*, 5326–5350. [CrossRef]
34. Phiri, D.; Morgenroth, J. Developments in Landsat Land Cover Classification Methods: A review. *Remote Sens.* **2017**, *9*, 967. [CrossRef]
35. Amini, S.B.; Saber, M.; Rabiei-Dastjerdi, H.; Homayouni, S. Urban Land Use and Land Cover change Analysis using random forest classification of landsat Time Series. *Remote Sens.* **2022**, *14*, 2654. [CrossRef]
36. Chander, G.; Markham, B.L.; Helder, D.L. Summary of current radiometric calibration coefficients for LaNdsAT MSS, TM, ETM+, and EO-1 ALI sensors. *Remote Sens. Environ.* **2009**, *113*, 893–903. [CrossRef]
37. Zhu, Z.; Wulder, M.A.; Roy, D.P.; Woodcock, C.E.; Hansen, M.C.; Radeloff, V.C.; Healey, S.P.; Schaaf, C.B.; Hostert, P.; Strobl, P.; et al. Benefits of the Free and Open Landsat Data Policy. *Remote Sens. Environ.* **2019**, *224*, 382–385. [CrossRef]
38. Cohen, W.B.; Goward, S.N. Landsat's role in Ecological Applications of Remote Sensing. *BioScience* **2004**, *54*, 535. [CrossRef]
39. Koschke, L.; Fürst, C.; Frank, S.; Makeschin, F. A multi-criteria approach for an integrated land-cover-based assessment of ecosystem services provision to support landscape planning. *Ecol. Indic.* **2012**, *21*, 54–66. [CrossRef]
40. Madanian, M.; Soffianian, A.; Koupai, S.S.; Pourmanafi, S.; Momeni, M. Analyzing the effects of urban expansion on land surface temperature patterns by landscape metrics: A case study of Isfahan City, Iran. *Environ. Monit. Assess.* **2018**, *190*. [CrossRef]
41. Oshiro, T.M.; Perez, P.S.; Baranauskas, J.A. *How Many Trees in a Random Forest?* Lecture Notes in Computer Science; Springer: Berlin/Heidelberg, Germany, 2012; pp. 154–168. [CrossRef]
42. Breiman, L. Bagging predictors. *Mach. Learn.* **1996**, *24*, 123–140. [CrossRef]
43. James, G.; Witten, D.; Hastie, T.; Tibshirani, R. *An Introduction to Statistical Learning*; Springer Texts in Statistics; Springer: Berlin/Heidelberg, Germany, 2013. [CrossRef]
44. Hastie, T.; Tibshirani, R.; Friedman, J.H. *The Elements of Statistical Learning*; Springer Series in Statistics; Springer: Berlin/Heidelberg, Germany, 2001. [CrossRef]
45. Schultz, B.; Immitzer, M.; Formaggio, A.R.; Sanches, I.D.; Luiz AJ, B.; Atzberger, C. Self-Guided Segmentation and Classification of Multi-Temporal LandsAt 8 images for crop type mapping in southeastern Brazil. *Remote Sens.* **2015**, *7*, 14482–14508. [CrossRef]
46. Duro, D.C.; Franklin, S.E.; Dubé, M.G. A comparison of pixel-based and object-based image analysis with selected machine learning algorithms for the classification of agricultural landscapes using SPOT-5 HRG imagery. *Remote Sens. Environ.* **2012**, *118*, 259–272. [CrossRef]
47. Stefanski, J.; Mack, B.; Waske, B. Optimization of Object-Based image analysis with random forests for land cover mapping. *IEEE J. Sel. Top. Appl. Earth Obs. Remote Sens.* **2013**, *6*, 2492–2504. [CrossRef]
48. Breiman, L. Classification and regression trees. *Biometrics* **1984**, *40*, 874. [CrossRef]
49. Gomes CM, A.; Lemos, G.C.; Jelihovschi, E.G. Comparing the predictive power of the CART and CTREE algorithms. *Avaliaçao Psicol.* **2020**, *19*, 87–96. [CrossRef]
50. Sathyadevi, G. Application of CART algorithm in hepatitis disease diagnosis. In Proceedings of the International Conference on Recent Trends in Information Technology (ICRTIT), Chennai, India, 3–5 June 2011. [CrossRef]
51. Khatami, R.; Mountrakis, G.; Stehman, S.V. A Meta-analysis of remote sensing research on supervised pixel-based land-cover image classification processes: General guidelines for practitioners and future research. *Remote Sens. Environ.* **2016**, *177*, 89–100. [CrossRef]
52. Rujoiu-Mare, M.; Olariu, B.; Mihai, B.; Nistor, C.; Săvulescu, I. Land cover classification in Romanian Carpathians and Subcarpathians using multi-date Sentinel-2 remote sensing imagery. *Eur. J. Remote Sens.* **2017**, *50*, 496–508. [CrossRef]
53. Pontius, R.G.; Millones, M. Death to Kappa: Birth of quantity disagreement and allocation disagreement for accuracy assessment. *Int. J. Remote Sens.* **2011**, *32*, 4407–4429. [CrossRef]
54. Adelabu, S.; Mutanga, O.; Adam, E. Testing the reliability and stability of the internal accuracy assessment of random forest for classifying tree defoliation levels using different validation methods. *Geocarto Int.* **2015**, *30*, 810–821. [CrossRef]
55. Liu, C.; Frazier, P.; Kumar, L. Comparative assessment of the measures of thematic classification accuracy. *Remote Sens. Environ.* **2007**, *107*, 606–616. [CrossRef]
56. Olofsson, P.; Foody, G.M.; Stehman, S.V.; Woodcock, C.E. Making better use of accuracy data in land change studies: Estimating accuracy and area and quantifying uncertainty using stratified estimation. *Remote Sens. Environ.* **2013**, *129*, 122–131. [CrossRef]
57. Jensen, J.R.; Lulla, K. Introductory Digital Image Processing: A Remote Sensing Perspective. *Geocarto Int.* **1987**, *2*, 65. [CrossRef]
58. Zanaga, D.; Van De Kerchove, R.; De Keersmaecker, W.; Souverijns, N.; Brockmann, C.; Quast, R.; Wevers, J.; Grosu, A.; Paccini, A.; Vergnaud, S.; et al. *ESA WorldCover 10 m 2020 v100*; Zenodo: Geneva, Switzerland, 2021. [CrossRef]
59. Dierckx, W.; Sterckx, S.; Benhadj, I.; Livens, S.; Duhoux, G.; Van Achteren, T.; François, M.; Mellab, K.; Saint, G. PROBA-V Mission for Global Vegetation Monitoring: Standard products and image quality. *Int. J. Remote Sens.* **2014**, *35*, 2589–2614. [CrossRef]

60. Dwyer, J.L.; Roy, D.P.; Sauer, B.; Jenkerson, C.B.; Zhang, H.K.; Lymburner, L. Analysis Ready Data: Enabling analysis of the Landsat Archive. *Remote Sens.* **2018**, *10*, 1363. [CrossRef]
61. Buchhorn, M.; Smets, B.; Bertels, L.; De Roo, B.; Lesiv, M.; Tsendbazar, N.; Li, L.; Tarko, A. *Copernicus Global Land Service: Land Cover 100m: Version 3 Globe 2015-2019: Product User Manual*; Zenodo: Geneva, Switzerland, 2020. [CrossRef]
62. Sobrino, J.A.; Irakulis, I. A Methodology for Comparing the Surface Urban Heat Island in Selected Urban Agglomerations Around the World from Sentinel-3 SLSTR Data. *Remote Sens.* **2020**, *12*, 2052. [CrossRef]
63. Yu, Z.; Guo, X.; Jørgensen, G.; Vejre, H. How can urban green spaces be planned for climate adaptation in subtropical cities? *Ecol. Indic.* **2017**, *82*, 152–162. [CrossRef]
64. Maimaitiyiming, M.; Ghulam, A.; Tiyip, T.; Pla, F.; Carmona, P.; Halik, Ü.; Sawut, M.; Caetano, M. Effects of green space spatial pattern on land surface temperature: Implications for sustainable urban planning and climate change adaptation. *ISPRS J. Photogramm. Remote Sens.* **2014**, *89*, 59–66. [CrossRef]